14th International Symposium on Particle Image Velocimetry – ISPIV 2021
August 1–5, 2021

Time Resolved PIV of the Flow Field underneath an accelerating meniscus

M. Ratz[1,2], D. Fiorini[2], A. Simonini[2], C. Cierpka[1], M. A. Mendez[2*]

[1] Technische Universität Ilmenau, Institute of Thermodynamics and Fluid Mechanics, Ilmenau, Germany

[2] von Karman Institute for Fluid Dynamics, Enviromental and Applied Fluid Mechanics Department, Brussels, Belgium

[*] mendez@vki.ac.be

Abstract

We present an experimental analysis of the flow field near an accelerating contact line using time-resolved Particle Image Velocimetry (TR-PIV). Both advancing and receding contact lines are investigated. The analyzed configuration consists of a liquid column that moves along a vertical 2D channel, open to the atmosphere and driven by a controlled pressure head. Large counter-rotating vortices were observed and analyzed in terms of the maximum intensity of the Q-field. To compute smooth spatial derivatives and improve the measurement resolution in the post-processing stage, we propose a combination of Proper Orthogonal Decomposition (POD) and Radial Basis Functions (RBF). The RBFs are used to regress the spatial and temporal structures of the leading POD modes, so that "high-resolution" modes are obtained. These can then be combined to reconstruct high-resolution fields that are smooth and robust against measurement noise and amenable to analytic differentiation. The results show significant differences in the flow topology between the advancing and the receding cases despite velocity and acceleration of contact lines are comparable in absolute values. This suggests that the flow dynamics are tightly linked to the shape of the interface, which significantly differs in the two cases.

1 Introduction

The dynamics of a gas-liquid interface moving along a solid wall plays an essential role in many wetting/dewetting processes (e.g. inkjet printing), coating applications (e.g. slot die coating) and capillary driven flows (e.g. liquid absorption in porous media or liquid pumping in microgravity).

The capillary force plays a major role in these processes. This force depends on the curvature of the interface, which is linked to the angle formed at the contact line, known as contact angle. Two main challenges exists in the modelling of these flows. First, the value of the contact angle cannot be predicted in the continuous fluid mechanics framework: on the contrary, this is a necessary boundary condition that must be imposed to solve for the interface shape, and hence for the fluid flows on both the gas and the liquid sides. The most common solution to the problem is the implementation of empirical and semi empirical correlations for the (macroscopic) contact angle as a function of the contact line velocity (Hoffman, 1975; Kistler, 1993). The limitations of these formulations are described in Fiorini et al. (2021).

The second challenge is that the very notion of moving contact line is at odds with the notion of no-slip boundary conditions that viscosity imposes to the liquid close to the contact line. This is the well known hydrodynamic paradox, which has motivated many theoretical and experimental works on the flow field near moving contact lines. A solution to this paradox has been proposed by Huh and Scriven (1971), who described the flow motion sufficiently close to the contact line as a creeping flow obeying the biharmonic equation. Within this theory, the velocity fields compatible with advancing or receding contact lines for the case of wetting fluid configuration ($\theta < 90^o$) are characterised by a splitting streamline as sketched in Figure 1. In an advancing contact line (see Figure 1(a)), the fluid required to displace the interface is injected from the bulk (split injection configuration) while the opposite occurs in a receding contact line (split ejection configuration, see Figure 1(b)). Only few experimental investigation of these flow patterns have been presented (Fuentes and Cerro (2005); Nasarek et al. (2008); Zimmerman et al. (2010)) in the literature, mostly focused on quasi steady conditions.

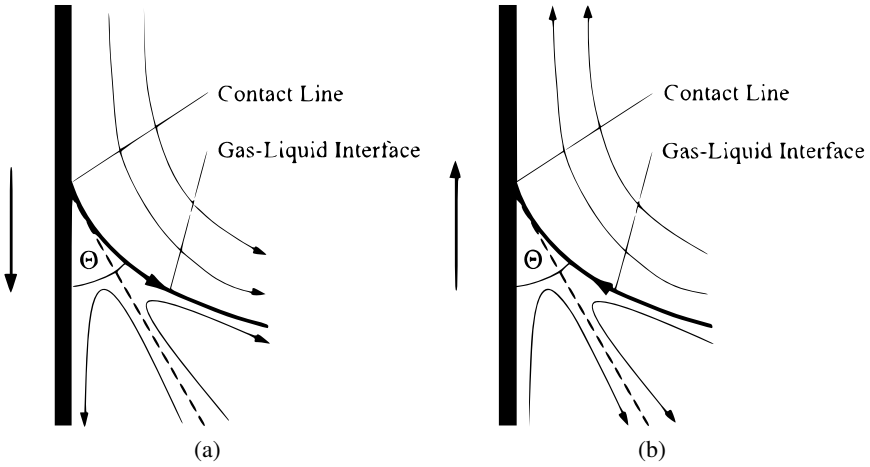

Figure 1: Schematic sketch of the stream lines in proximity of the contact line for a wetting configuration ($\theta < 90^o$) in case of an advancing contact line (left) and a receding contact line (right). The flow pattern on the left is known as *stream line split injection*, the flow pattern on the right is known as *stream line split ejection*. Images are taken from Fuentes and Cerro (2005).

While sufficiently close to the contact line the dominance of viscosity gives a sound theoretical justification to these patterns, it remains unclear what is their macroscopic impact on the dynamics of the interface and on the flow field far from it. At large Reynolds number or in the presence of strong acceleration, i.e. when inertia becomes important, the flow field sketched in Figure 1 might exist only very close to the interface but still have a strong impact to the flow at larger distances.

The practical implications are numerous, especially considering that flow field and contact angle are intimately linked (see Savelski et al. (1995)). In the classic capillary rise problem, for example, the most common models are based on the assumption that the flow field is fully developed (Washburn, 1921; Levine et al., 1976; Quéré, 1997), but no theoretical nor empirical law can identify the distance from the interface below which this assumption ceases to be valid (see Nasarek et al. (2008)).

This work presents an experimental investigation of the flow field near a contact line moving at relatively high velocities and subject to large accelerations. The configuration of interest is a narrow rectangular channel in which a vertical column of liquid is driven into motion by a controlled pressure step. The gas liquid interface in contact with the walls produces two dynamic menisci which forces the interface to form two dynamic contact angles. Both advancing and receding configurations are investigated.

The flow field was measured via time-resolved Particle Image Velocimetry (TR-PIV), in a region of interest that follows the interface in its displacement. The measurement reveal the formation of two large counter rotating vortices with time-varying intensity. The estimation of the vortex intensity was carried out in terms of Q-field (Hunt et al., 1988).

To accurately compute the required spatial derivatives, the velocity field is interpolated using a combination of Proper Orthogonal Decomposition (POD) and Radial Basis Function (RBF) regression. This approach was first proposed by (Karri et al., 2009; Raben et al., 2012) to compute spatial derivatives, and it is used here also for super-resolution. In particular, the RBF is used to smooth, filter and interpolate the spatial and temporal structures of the POD modes. The velocity field obtained from the reconstruction of the high-resolution POD modes enables super-resolution with robust outlier removal and analytic calculation of spatial and temporal derivatives. An adaptation of the tool for computing pressure field is currently in preparation (Sperotto et al., 2021). The method is reminiscent of Kriging enhanced gappy POD (Gunes et al., 2006), but differs in the use of the RBF as opposed to the kernel-based Kriging.

Section 2 shows the configuration of the narrow, two-dimensional channel in which the flow beneath the dynamic contact lines is observed. Section 3 presents the data processing for the PIV interrogation as well as the proposed regression tool. This algorithm is applied to a simple test case in Section 4.1 and compared to traditional interpolation methods. The experimental results are discussed in Section 4.2 and conclusions are given in Section 5.

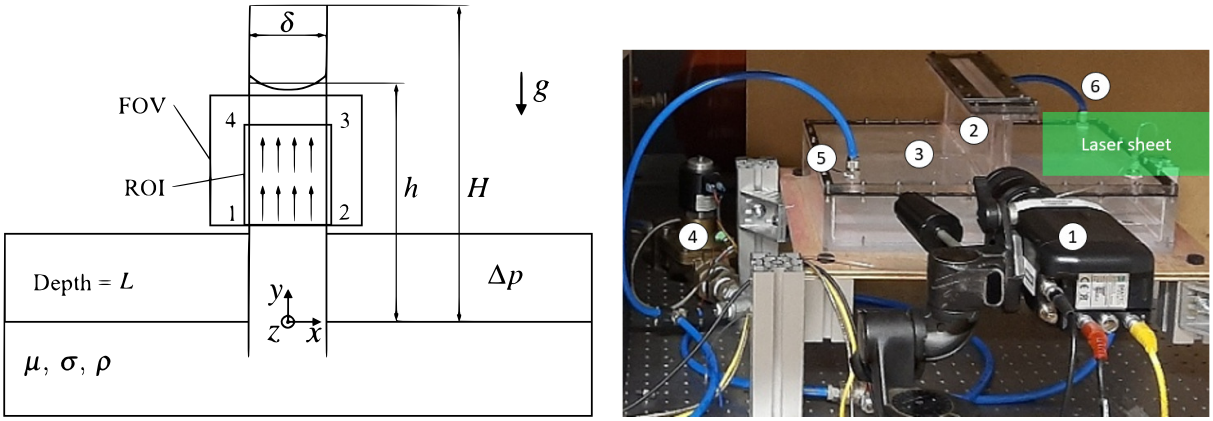

Figure 2: Fig (a) Sketch of the channel showing the area of the TR-PIV measurements. Fig (b) Picture of the experimental setup with the camera (1), the channel (2), the reservoir (3), the release valve (4) and the pressure ports (5 and 6).

2 Experimental Setup and Test Cases

A sketch of the experimental setup is shown in Figure 2a. This consists of a rectangular channel with a width of $\delta = 5$ mm much smaller than its depth $L = 250$ mm. The channel height is $H = 150$ mm and is open to atmosphere.

This channel is connected to a pressurized chamber in the bottom, sustaining the flow via a pressure difference Δp. To reproduce an advancing contact line (i.e. interface moving upwards, along the y-axis), a positive pressure difference Δp is suddenly introduced in the chamber by the opening of a fast release electronic valve connected to a pressure line. This valve opens linearly in 0.2 s. To reproduce a receding contact line (i.e. interface moving downward), the opposite procedure is followed: the chamber is initially at a Δp= 1200 Pa and the release valve is suddenly opened to the atmosphere, resulting in $\Delta p = 0$ Pa.

A picture of the experimental setup is shown in Figure 2b. The camera is placed perpendicularly to the channel's flow cross section and illuminated with a laser sheet from the right side. The injection/removal of air during the pressurisation/depressurisation used in the advancing/receding experiments is performed on two sides of the chamber in order to ensure a symmetric flow and to minimise the entry effects. Together with the camera (1), the picture shows the channel (2) and the pressurized chamber (3), the fast opening vale (4), and the two pressure ports (5 and 6).

Water is used as a fluid and the walls are made of plexiglass. The fluid is seeded with *Red Fluorescent Polymer Microspheres* from *Thermo Fisher Scientific* with a diameter of 12 µs. The flow is observed with a TR-PIV system from Dantec dynamics. The particles are illuminated with the laser (DM40-527-DH Nd: YLF from Photonics Industries) with a wavelength of 527 µm and a maximum pulse energy of 40 mJ at a frequency of 1 kHz. Images are recorded with a SpeedSense Ethernet M310 camera having a resolution of 1280×800 px at a maximum frame rate of 3260 Hz. An objective lens with a focal length of 105 mm is used to get an optical magnification of 60 px/mm.

The images are acquired in single frame mode using the Dantec's software Dynamic Studio. The exposure time of the camera is set to 250 s and the frame rate is set to 1200 Hz. The time resolved configuration allows to capture about 60 snapshots during the rising/advancing experiment and about 100 during the descending/receding experiments

For the rising interface, the flow is observed at the very top of the channel, close to the maximum height. In the first case, the reservoir is at an initial pressure of 0 Pa and the pressure difference is 1500 Pa. This is referred to as 'Test Cases 1'. The second case, referred to as 'Test Case 2', has an initial pressure of 200 Pa, the pressure difference is 1200 Pa. These different initial conditions result in the same final height of the meniscus. The descending interface is observed at multiple positions inside the channel by changing the height of the camera between measurements. Additionally, the release speed of the liquid is varied between cases to investigate the effects of different accelerations. The release speed is controlled by opening the release valve to the surrounding air at different speeds.

3 Data Processing: Smoothing, Super-Resolution and Q-Fields

The PIV images are pre-processed using the POD-based background removal introduced by Mendez et al. (2017). The PIV interrogation is carried out using an in-house adaptation of *OpenPIV* (Liberzon et al., 2020).

In particular, due to the nature of the flow, two additional features were implemented. First, because of the large aspect ratio of the flow (the velocity component v, along y, is much larger than the velocity component u, along x), rectangular interrogation windows were implemented. This allows for a better sampling of the flow in the direction where the most substantial gradients are expected without deteriorating the signal-to-noise ratio in the cross-correlation maps.

The second implementation is a dynamic Region of Interest (ROI) to follow the gas-liquid interface across the available Field of View (FOV), as schematically illustrated in Figure 2(a). At each image pair k at time t_k, the velocity profile along the edge 1-2 (denoted as $y_{1,2}$) is used to compute the average velocity $\overline{v}_k = \int_{-\delta/2}^{\delta/2} v(x, y_{1,2}, t_k) dx$ and displace vertically the FOV in the following image pair by $\overline{v}\Delta t$. This allows focusing the processing always in the same region below the interface.

Adaptive iterative multigrid interrogation (Scarano and Riethmuller, 2000) is used to calculate the velocity fields. For the advancing contact line experiments, the initial window size is set to 256×64 px and reduced over two steps to 64×16 px. For the receding contact line experiments, the initial size is 64×64 px, and reduced to 24×24 px in two iterations. Outliers are removed based on the signal-to-noise ratio measured in terms of peak to standard deviation in the cross-correlation map.

The post-processing of the PIV fields begins with a POD-based filter using a classic truncation

$$\vec{u}(\mathbf{x}_0, t_0) = \sum_{i=1}^{R} \sigma_i \vec{\phi}_i(\mathbf{x}_0) \varphi_i(t_0)\,, \tag{1}$$

where $R \ll n_t$ is the truncation index, σ_i is the amplitude of the i-th POD mode having spatial structure $\vec{\phi}_i(\mathbf{x}_0)$ and temporal structure $\varphi_i(t_0)$. Note that $\mathbf{x}_0 \in \mathbb{R}^{n_s \times 1}$ and $t_0 \in \mathbb{R}^{n_t \times 1}$ here denote the spatial and temporal grids in which the PIV field is available, reshaped as column vectors for computational convenience. Because the flow fields here are bidimensional, given n_x and n_y the number of points along x and y, we have $n_s = 2n_x n_y$.

The spatial structures $\vec{\phi}(\mathbf{x}_0) = (\phi_u(\mathbf{x}_0), \phi_v(\mathbf{x}_0))$ collects the dominant velocity fields, computed by projecting the velocity field $\vec{u} = (u, v)$ on the POD temporal basis. The details of the POD computation can be found elsewhere (e.g. Mendez et al. (2019, 2020a)) and are thus omitted here. The main idea behind the super-resolution strategy developed in this work is to perform Radial Basis Function (RBFs, see Fornberg and Flyer (2015)) regression of the spatial and temporal structures of the decomposition, and then use a reconstruction of high-resolution POD modes to rebuild the velocity field. The RBF regression consists in writing both of these bases as linear combination of RBFs bases, i.e.:

$$\vec{\phi}_i(\mathbf{x}_0) = \sum_{j=1}^{n_\phi} w_{ij}^{\phi} \gamma_j^{\phi}(\mathbf{x}_0 | \mathbf{x}_{i,j}, \Sigma_{\phi_j}) \qquad \text{and} \quad \varphi_i(t_0) = \sum_{j=1}^{n_\varphi} w_{i,j}^{\varphi} \gamma_j^{\varphi}(t_0 | t_j, \Sigma_{\varphi_j})\,, \tag{2}$$

where $w_{i,j}^{\phi}$ and $w_{i,j}^{\varphi}$ are the set of weights defining the regression functions, $\gamma_j^{\phi}(\mathbf{x}_0|\mathbf{x}_j, \Sigma_{\phi_j})$ are the n_ϕ radial basis functions in space and $\gamma_j^{\varphi}(t_0|t_j, \Sigma_{\varphi_j})$ are the n_φ radial basis functions in time. These have collocation points $\mathbf{x}_j$ and t_j and shape parameters Σ_{ϕ_j} and Σ_{φ_j}. Note that the coefficients $w_{i,j}^{\phi}$ must be defined as vectors, i.e. $w_{i,j}^{\phi} = (w_{u,i,j}^{\phi}, w_{v,i,j}^{\phi})$ since the same radial basis γ_j^{ϕ} is used for both components (ϕ_u, ϕ_v). However, because every snapshot is reshaped as a column vector, regardless of whether this collects a vector or a scalar field, we keep the same notation as for the interpolation of the temporal structures.

In this work, we consider Gaussian RBF of the form:

$$\gamma_j^{\phi}(\mathbf{x}_0|\mathbf{x}_j, \Sigma_{\phi_j}) = \exp\left(-(\mathbf{x}_0 - \mathbf{x}_j)^T \begin{pmatrix} 1/2\sigma_x^2 & 0 \\ 0 & 1/2\sigma_y^2 \end{pmatrix} (\mathbf{x}_0 - \mathbf{x}_j) \right) \;;\; \gamma_j^{\varphi}(t_0|t_j, \Sigma_{\varphi_j}) = \exp\left(\frac{-(t_0 - t_j)^2}{\sigma_t^2} \right), \tag{3}$$

i.e. $\Sigma_{\phi_j} = diag(1/2\sigma_x^2, 1/2\sigma_y^2)$ and $\Sigma_{\varphi_j} = 1/2\sigma_t^2$. For both space and time regressions, the collocation point and the shape parameters are defined a priori and the regression is solved once the weights are identified. Reshaping all bases functions as columns of matrices $\Gamma_\phi(\mathbf{x}_0) \in \mathbb{R}^{n_s \times n_\phi}$ and $\Gamma_\varphi(t_0) \in \mathbb{R}^{n_t \times n_\varphi}$, collecting all

the unknown weights into column vectors $\mathbf{w}^{\phi} \in \mathbb{R}^{n_\phi \times 1}$, $\mathbf{w}^{\varphi} \in \mathbb{R}^{n_\phi \times 1}$ and collecting all the entries of $\vec{\phi}_i(\mathbf{x}_0)$ and $\varphi_i(t_0)$ into column vectors $\phi_0 \in \mathbb{R}^{n_s \times 1}$ and $\varphi_0 \in \mathbb{R}^{n_t \times 1}$, the weights are solution of classic least square problems. Using a standard Tikhonov regularization to mitigate the risks of overfitting (Mendez et al., 2020b), the solution reads:

$$\mathbf{A}\mathbf{x} = \mathbf{b} \quad \rightarrow \mathbf{x} = \left(\mathbf{A}^T\mathbf{A} + \alpha\mathbf{I}\right)^{-1}\mathbf{A}^T\mathbf{b}, \tag{4}$$

where $\mathbf{A} = \Gamma_\phi(\mathbf{x}_0)$, $\mathbf{x} = \mathbf{w}^{\phi}$ and $\mathbf{b} = \phi_i$ for the regression in space and $\mathbf{A} = \Gamma_\varphi(t_0)$, $\mathbf{x} = \mathbf{w}^{\varphi}$ and $\mathbf{b} = \varphi_i$ for the regression in time. The regularization parameter α is taken as $\varepsilon||\mathbf{A}||_F$, with $\varepsilon = 1e-11$ and $||A||_F$ the Frobenious norm of $\mathbf{A}$. Note that the inverse in equation 4 can be precomputed and the system solved for all the modes in a single step.

Once the weights are computed, equation (2) can be used on any arbitrary mesh grid $\mathbf{x}$ and any time discretization t. Then, the interpolated field reads

$$\vec{u}(\mathbf{x},t) = \sum_{i=1}^{R} \sigma_i \vec{\phi}_i(\mathbf{x})\varphi_i(t) \quad \text{with} \quad \begin{cases} \vec{\phi}_i(\mathbf{x}) = \sum_{j=1}^{n_\phi} w_j^{\phi}\gamma_j^{\phi}(\mathbf{x}|\mathbf{x}_j, \Sigma_{\phi_j}) \\ \varphi_i(t) = \sum_{j=1}^{n_\varphi} w_j^{\varphi}\gamma_j^{\varphi}(t|t_j, \Sigma_{\varphi_j}) \end{cases} \tag{5}$$

The derivatives of the flow can now be computed analytically by simply replacing the RBF with their required partial derivatives. For example, the spatial derivative $\partial_x u$ can be computed as:

$$\partial_x u(\mathbf{x},t_k) = \partial_x\left(\sum_{i=1}^{R}\sigma_i\phi_{u,i}(\mathbf{x})\varphi_i(t_k)\right) = \sum_{i=1}^{R}\sigma_i\partial_x\phi_{u,i}(\mathbf{x})\varphi_i(t_k) \quad \text{with} \quad \partial_x\phi_{u,i}(\mathbf{x}) = \sum_{j=1}^{n_\phi} w_j^{\phi}\partial_x\gamma_j^{\phi}(\mathbf{x}|\mathbf{x}_j, \Sigma_{\phi_j}). \tag{6}$$

This derivative is analytically available because $\partial_x\gamma_j^{\phi}$ is analytically available by differentiating eq.3. Finally, as all derivatives can be accurately computed, the strength of the vortices detected in the PIV fields can be measured in terms of Q-field (Hunt et al., 1988)

$$Q = \frac{1}{2}(||\Omega||_F^2 - ||S||_F^2) = -\frac{1}{2}\left((\partial_x u)^2 + 2\partial_y u\,\partial_x v + (\partial_y v)^2\right) \tag{7}$$

where $S = 1/2(\nabla V + \nabla V^T)$ and $\Omega = 1/2(\nabla V - \nabla V^T)$ the symmetric and anti symmetric portions of the velocity gradient tensor.

4 Results

4.1 Synthetic Test Case

Before analysing the experimental data, we consider a simple synthetic test case to test the robustness of the implemented RBF regression against noise. The flow field chosen for the test is $\vec{u} = (u,v) = (\sin(\mathrm{x}) \cdot \cos(\mathrm{y}), -\cos(\mathrm{x}) \cdot \sin(\mathrm{y}))$ over a domain $\mathbf{x} = [0,\pi] \times [0,\pi]$. This field is sampled on a Cartesian grid with $n_x = n_y = 11$ points and is shown in Figure 3(a).

To simulate different noise levels, we add a white noise field $\vec{w}(\mathbf{x}) \in [0,1]$ with relative intensity p, i.e. $\vec{u}_\delta(\mathbf{x}) = \vec{u}(\mathbf{x})(1 + p\vec{w}(\mathbf{x}))$. The perturbed fields with $p = 0.5$ and $p = 1$ are shown in Figures 3(b) and 3(c) respectively.

The spatial regression is performed using a total of $n_\Phi = 40 \times 40$ Gaussian RBFs (see eq 3) with $\sigma_x = \sigma_y = 2$. The collocation points are uniformly distributed over a Cartesian grid in the domain $\mathbf{x}$. The RBF regression is then used to re-sample the velocity field onto a much finer grid, i.e. $n_x = n_y = 22$. The results for the three fields in Figures 3(a), 3(b) and 3(c) are shown in Figures 3(d), 3(e) and 3(f) respectively.

In all these cases, the RBF regression removes the noise and reconstructs the flow field on the much finer grid. We close this subsection by comparing the performances of the RBF regression with two classic interpolants: a linear interpolation and a cubic spline interpolation, as available from the Python's library Scipy. The performances were evaluated in terms of Mean Absolute Error (MAE), defined as:

$$MAE = \frac{1}{n_x n_y}\sum_{i=1}^{n_x \cdot n_y} |v_{GT,i} - v_i| \tag{8}$$

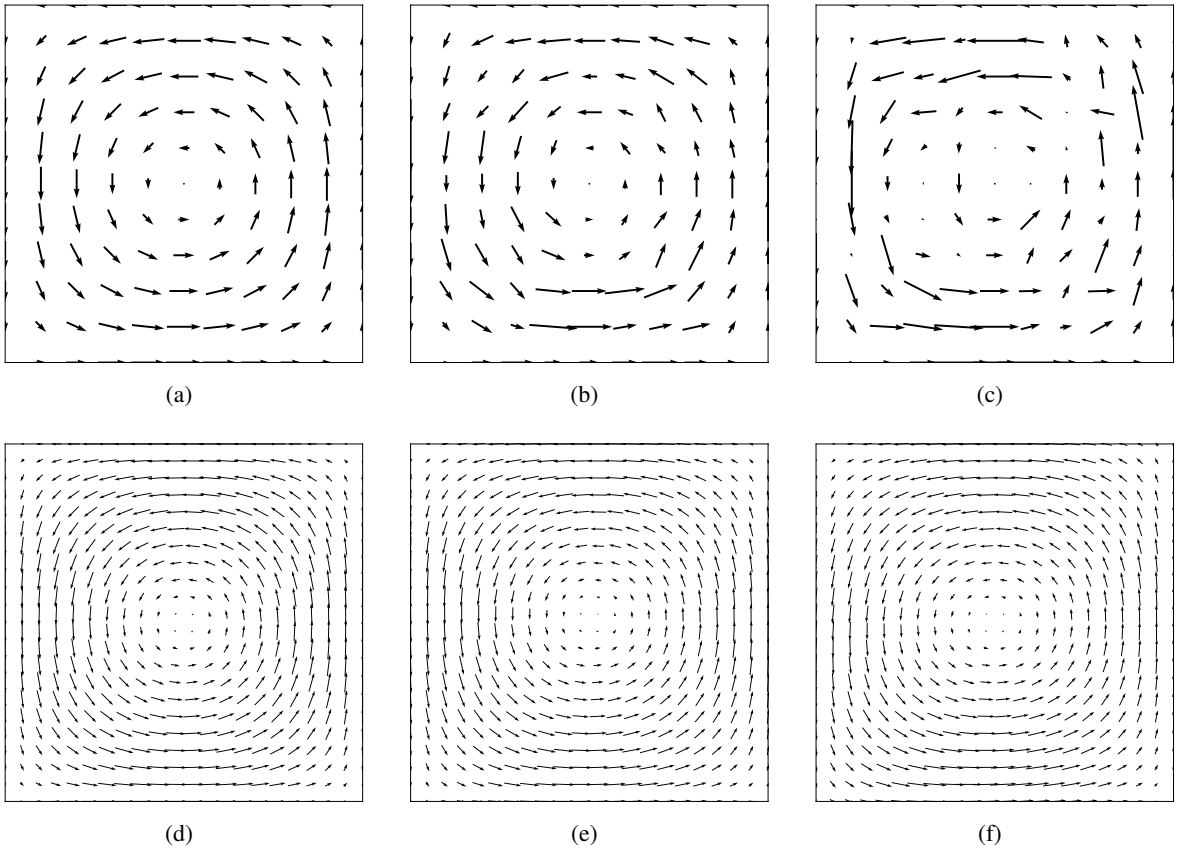

Figure 3: Illustrative synthetic test case to analyze the robustness of the RBF regression: a vortex field is sampled over a coarse grid. Fig (a) - (c): velocity field on the coarse grid with noise level (defined in the text) $p = 0, 0.5, 1$. Fig (d)-(f): results of the re-sampling of the RBF regression on a much finer grid for the cases (a)-(c).

Where v_i is the prediction of the interpolant and $v_{GT,i}$ is the analytic flow field. The results are shown in Figure 4 as a function of the noise parameter p. While at low levels of noise the three approaches are comparable, the RBF is significantly more robust as p is increased.

4.2 PIV Fields

The PIV velocity fields were processed retaining a total of $R = 25$ POD modes in equation (1). The temporal structures of the modes were approximated with $n_\varphi = 500$ RBFs with $\sigma_t = 0.01$ while $n_\phi = 900$ RBFs were used for the spatial structures (see equation (3)). For the regression in space, the RBFs were collocated over a regular grid of $n_{Bx} \times n_{By} = 60 \times 15$ and anisotropic kernels with $\sigma_x = 10$ and $\sigma_y = 15$ were selected. This allows to efficiently account for the high aspect ratio of the flow. No re-sampling was performed in the time domain since the available time resolution was sufficient for the scope of this work.

The spatial resolution of the PIV field, i.e. $\mathbf{x}_0$ in equation (1)-(3), has a resolution of $\Delta x = 0.12\,\text{mm}$ and $\Delta y = 0.48\,\text{mm}$ for the rising test cases and a resolution of $\Delta x = \Delta y = 0.22\,\text{mm}$ for the descending test cases. The resulting RBF regression is used to re-sample the velocity field over a grid ($\mathbf{x}$ in equation (5)) with a resolution of $\Delta x = 0.04\,\text{mm}$ and $\Delta y = 0.16\,\text{mm}$ for the rising test casess, and $\Delta x = \Delta y = 0.07\,\text{mm}$ for the descending test cases.

Figure 5 shows the results of the experiments with the rising interface, i.e. the advancing contact line problem. Figure 5(a) and 5(b) show the acceleration and the maximum Q-field within the ROI as a function of the mean velocity within the channel. The labels correspond to the ones explained in Section 2. The mean velocity is calculated by zero padding the velocity field at the walls and taking the mean of the average velocity of the bottom five rows and the acceleration is computed from the time derivative of the mean

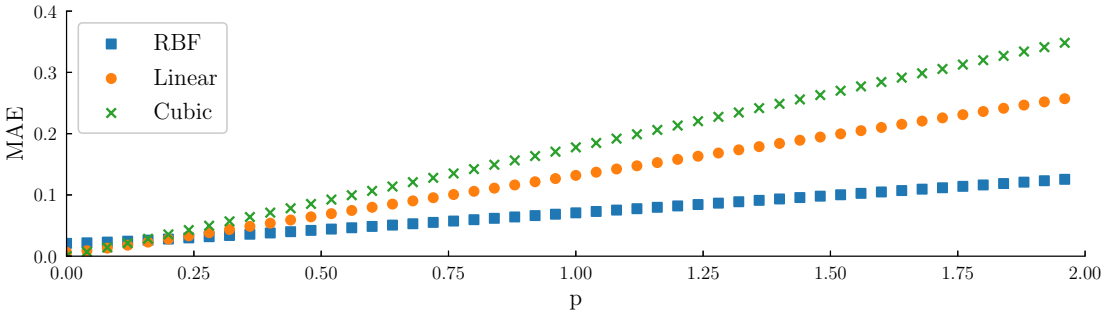

Figure 4: Mean absolute error after interpolation over the level of noise. 'RBF' refers to the implemented interpolator, 'linear' and 'cubic' an interpolator using bivariate splines of first and third order.

velocity. A clear trend is visible: the Q-field is increasing with decreasing mean velocity.

Three instantaneous velocity fields are shown in Figures 5(c) - 5(e), corresponding to the three points marked in Figure 5(a) and 5(b). For plotting purposes, the velocity fields are slightly high-pass filtered by using a Gaussian filter with $\sigma_x = \sigma_y = 15$ and a truncation after 2.5 standard deviations. The quiver plot only shows every second column for the rising interface to avoid overcrowding the image. The Q-field is also shown in each snapshot for quantitative analysis and the axis aspect ratio is set to one. The upper horizontal boundary of the ROI is placed approximately 0.2 mm from the interface at the center of the channel, and this is the case for the three shown snapshots. However, because of light reflections and diffraction some of the rows close to the interface are sometimes considered invalid and hence this distance increases up to 1.5 mm. This might explain the noisy trends in Figure 5(a) and 5(b).

In each case, two counter rotating vortices are visible close to the walls. The one on the right is rotating clockwise and the one on the left counterclockwise. The vortices extends considerably along the vertical direction but only over a small distance in the cross-stream direction. At a distance of 1 mm from the wall, these have no appreciable influence on the velocity field.

The initial pressure was high enough to produce a strong acceleration, as shown in Figure 5(a). While the rolling motion of the flow is still present, the significant acceleration and high velocities push the stream-line split injection pattern and its vortices towards the wall.

It is worth noticing that the velocity fields look similar even though Figure 6(c) and 6(d) have largely different accelerations. Referring to the expected theoretical flow field from Figure 1(a), it appears that the stream-line split injection forms a small angle with the walls. As a result, the rolling motion expected by the viscous-capillary balance is confined to a narrow region of the flow.

Figure 6 shows the same results for the cases with the descending interface. The velocities and accelerations in Figure 6(a) and 6(b) have a different sign because the interface moves downward. A similar trend as for the rising interface can be observed, with the magnitude of the Q-field increasing as the velocity decreases. However, the reader should note that a decreasing velocity in this case means that the absolute value of the velocity is increasing. Another observation is the increased strength of the Q-field, with the maximum value being almost an order of magnitude above the maximum value for the rising interface.

The vortices in Figure 6(c) - 6(e) show a different behaviour than the ones for the rising interface. Besides the reversed rotation, as expected from the theoretical flow topology in Figure 1, their centre is much closer to the centre of the channel, and the rolling motion extends much further in both the x and y-direction. In the case of the receding contact line, the stream-line split ejection (see Figure 1(b)) forms a larger angle with the wall than for the advancing contact line.

The large difference cannot be justified by the velocity of the contact line, which in the slowest rising test cases is comparable to the fastest falling test cases, nor by its acceleration, which are also comparable in the cases in 6(c) and the one in Figure 5(e).

5 Conclusions and Perspectives

Time-Resolved PIV measurements of the flow field underneath a dynamic meniscus have been carried out in a two-dimensional channel. Both advancing and receding contact lines were investigated. In both cases, two counter-rotating vortices were observed below the meniscus. In addition, super-resolution of the velocity

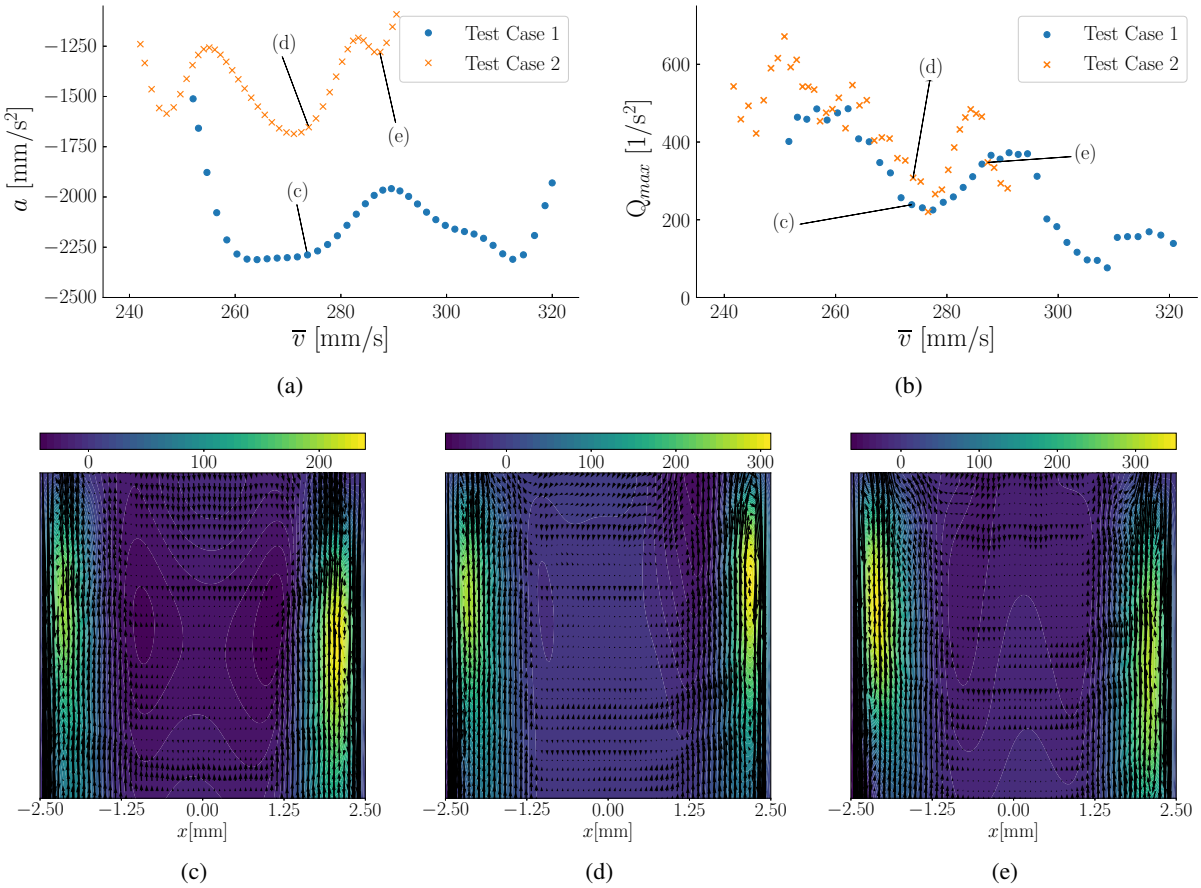

Figure 5: Results for the rising interface. Fig (a) - (b) Acceleration and maximum Q-field over the mean velocity for different test cases. The blue case corresponds to an initial pressure of 1400 Pa and the orange one to 1500 Pa. Fig (c) - (e) Q-field contour with the high-pass filtered velocity field. The aspect ratio of the plot is set to one.

fields was achieved using a regression scheme that combines an analytic approximation of the spatial and temporal structures of the leading POD modes using RBFs. This allowed analytical differentiation and accurate computation of the Q-fields.

In both advancing and receding cases, the strength of the vortices depends on the mean velocity and the acceleration of the flow, and whether the contact line is advancing or receding. The latter is especially important because the splitting stream-line forms a different angle with the wall and has the largest impact on the flow field.

Significant differences were observed between advancing/receding wetting configurations even when the modulus of velocity and acceleration of the contact lines were comparable. The main difference between the two cases was found in the interface's shape (not shown here): this appeared nearly flat in the advancing cases and characterized by large menisci, with small contact angles, during the receding test cases. Future work will complement the presented investigation with an analysis of the interface shape in both experiments.

Acknowledgments

This project was funded by Arcelormittal Maizières Research SA in the framework of the 'Minerva Project', and the authors thank Jean-Michel Mataigne for many fruitful discussions on dynamic wetting. D. Fiorini is supported by Fonds Wetenschappelijk Onderzoek (FWO), Project number 1S96120N.

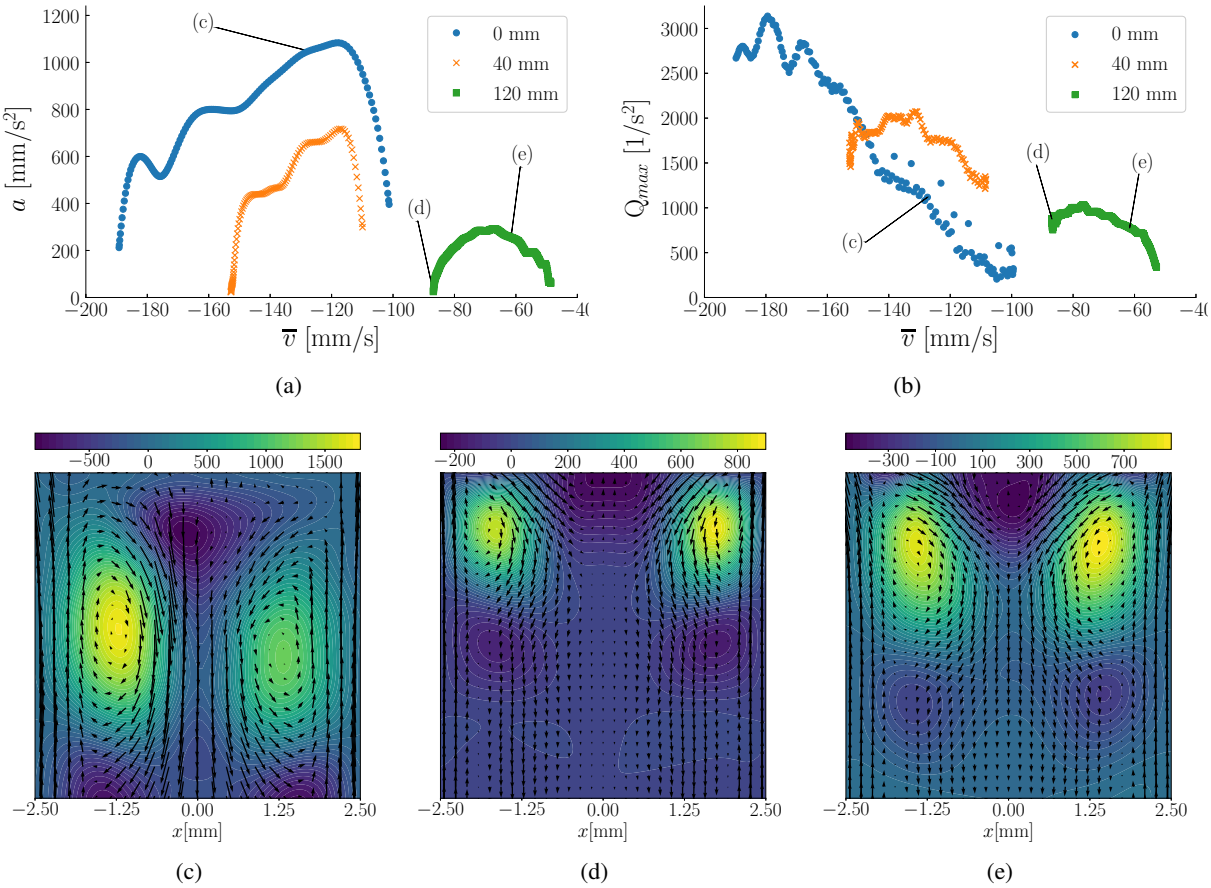

Figure 6: Results for the descending interface. Fig (a) - (b) Acceleration and maximum Q-field over the mean velocity for different test cases. The labels refer to the vertical position of the camera, where 0 mm refers to the part of the channel where it meets the reservoir. Fig (c) - (e) Q-field contour with the high-pass filtered velocity field. The aspect ratio of the plot is set to one.

References

Fiorini D, Mendez AM, Simonini A, Seveno D, and Johan S (2021) A study on the effect of inertia on dynamic contact angles using an inverse method. *to appear in Journal of colloid and interface science*

Fornberg B and Flyer N (2015) Solving pdes with radial basis functions. *Acta Numerica* 24:215–258

Fuentes J and Cerro R (2005) Flow patterns and interfacial velocities near a moving contact line. *Experiments in Fluids* 38:503–510

Gunes H, Sirisup H, and Karniadakis GE (2006) Gappy data: To krig or not to krig?. *Journal of Computational Physics 212* 212:358–382

Hoffman RL (1975) A study of the advancing interface. i. interface shape in liquid—gas systems. *Journal of Colloid and Interface Science* 50:228 – 241

Huh C and Scriven L (1971) Hydrodynamic model of steady movement of a solid/liquid/fluid contact line. *Journal of Colloid and Interface Science* 35:85–101

Hunt J, Wray A, and Moin P (1988) Eddies, streams, and convergence zones in turbulent flows. in *Studying Turbulence Using Numerical Simulation Databases, 2. Proceedings of the 1988 Summer Program, Stanford, California, USA, June 27 - July 22*

Karri S, Charonko J, and Vlachos P (2009) Robust wall gradient estimation using radial basis functions and proper orthogonal decomposition (pod) for particle image velocimetry (piv) measured fields. *Measurement Science and Technology* 20:045401

Kistler SF (1993) Hydrodynamics of Wetting. in *Wettability*. chapter 6, pages 311 – 430. CRC Press

Levine S, Reed P, Watson E, and Neale G (1976) A theory of the rate of rise of a liquid in a capillary. in *Colloid and interface science*. pages 403–419. Academic Press

Liberzon A, Lasagna D, Aubert M, Bachant P, Käufer T, jakirkham, Bauer A, Vodenicharski B, Dallas C, Borg J, tomerast, and ranleu (2020) Openpiv/openpiv-python: added synthetic image generator

Mendez M, Raiola M, Masullo A, Discetti S, Ianiro A, Theunissen R, and Buchlin J (2017) Pod-based background removal for particle image velocimetry. *Experimental Thermal and Fluid Science* 80:723–729

Mendez MA, Balabane M, and Buchlin JM (2019) Multi-scale proper orthogonal decomposition of complex fluid flows. *Journal of Fluid Mechanics* 870:988–1036

Mendez MA, Hess D, Watz BB, and Buchlin JM (2020a) Multiscale proper orthogonal decomposition (mPOD) of TR-PIV data—a case study on stationary and transient cylinder wake flows. *Measurement Science and Technology* 31:094014

Mendez MA, Pino F, and Fiore M (2020b) Machine learning for fluid mechanics: Challenges, opportunities and perspectives. in *Optimization Methods for Computational Fluid Dynamics, VKI Lecture Series*. von Karman Institute

Nasarek R, Wereley S, and Stephan P (2008) Flow Field Measurements Near a Moving Meniscus of a Capillary Flow With Micro Particle Image Velocimetry (μPIV). in *Proceedings of the Sixth International ASME Conference on Nanochannels, Microchannels and Minichannels, Darmstadt, Germany, June 23-25*

Quéré D (1997) Inertial capillarity. *Europhysics Letters* 39:533–538

Raben SG, Charonko JJ, and Vlachos PP (2012) Adaptive gappy proper orthogonal decomposition for particle image velocimetry data reconstruction. *Measurement Science and Technology* 23:025303

Savelski M, Shetty S, Kolb W, and Cerro R (1995) Flow patterns associated with the steady movement of a solid/liquid/fluid contact line. *Journal of Colloid and Interface Science* 176:117–127

Scarano F and Riethmuller M (2000) Pod-based background removal for particle image velocimetry. *Experiments in Fluids* 29:51–60

Sperotto P, Mendez M, and Pieraccini S (2021) A meshless method to measure pressure fields via radial basis functions. *to appear in Experiments in Fluids*

Washburn EW (1921) The dynamics of capillary flow. *Physical Review* 17:273–283

Zimmerman J, Weislogel M, and Tretheway D (2010) Micro-PIV Measurements near a Moving Contact Line. in *Proceedings of the ASME 2010 International Mechanical Engineering Congress & Exposition, Vancouver, British Columbia, Canada, November 12-18*